





Article

Extraordinary Response of H-Charged and H-Free Coherent Grain Boundaries in Nickel to Multiaxial Loading

Petr Šesták ^{1,*} , Miroslav Černý ^{1,2} , Zhiliang Zhang ³  and Jaroslav Pokluda ^{1,2,4} 

¹ Central European Institute of Technology, CEITEC BUT, Brno University of Technology, Purkyňova 123, CZ-612 00 Brno, Czech Republic; cerny.m@fme.vutbr.cz (M.Č.); pokluda@fme.vutbr.cz (J.P.)

² Faculty of Mechanical Engineering, Brno University of Technology, Technická 2896/2, CZ-616 69 Brno, Czech Republic

³ Faculty of Engineering, Norwegian University of Science and Technology (NTNU), Rich. Birkelandsvei 1A, 7491 Trondheim, Norway; zhiliang.zhang@ntnu.no

⁴ Faculty of Special Technology, Alexander Dubcek University of Trencin, Pri parku 19, 911 06 Trenčín, Slovakia

* Correspondence: petr.sestak@ceitec.vutbr.cz

Received: 29 May 2020; Accepted: 6 July 2020; Published: 8 July 2020



Abstract: The cohesive strength of $\Sigma 3$, $\Sigma 5$, and $\Sigma 11$ grain boundaries (GBs) in clean and hydrogen-segregated fcc nickel was systematically studied as a function of the superimposed transverse biaxial stresses using ab initio methods. The obtained results for H-free GBs revealed a quite different response of the coherent twinning boundary $\Sigma 3$ to the applied transverse stresses in comparison to the other GB types. While the cohesive strength of $\Sigma 5$ and $\Sigma 11$ GBs increased with increasing level of tensile transverse stresses, the strength of $\Sigma 3$ GB remained constant for any applied levels of transverse stresses. In the case of GBs with segregated hydrogen, the cohesive strength of $\Sigma 3$ was distinctly reduced for all levels of transverse stresses, while the strength reduction of $\Sigma 5$ and $\Sigma 11$ GBs was significant only for a nearly isotropic (hydrostatic) triaxial loading. This extraordinary response explains a high susceptibility of $\Sigma 3$ GBs to crack initiation, as recently reported in an experimental study. Moreover, a highly triaxial stress at the fronts of microcracks initiated at $\Sigma 3$ boundaries caused a strength reduction of adjacent high-energy grain boundaries which thus became preferential sites for further crack propagation.

Keywords: ab initio calculations; hydrogen embrittlement; grain boundary; cohesive strength; multiaxial loading

1. Introduction

Hydrogen may cause a significant reduction of ductility of metallic materials which leads to a premature fracture of engineering components and structures. This so-called hydrogen embrittlement was already extensively studied in the last century with the help of experimental [1,2] as well as theoretical methods [3–13]. The most accepted theoretical concepts explaining the embrittlement at the atomistic level are the Hydrogen-Enhanced Decohesion (HEDE) [14] and the Hydrogen-Enhanced Localized Plasticity (HELP) [15]. The HEDE concept deals with a hydrogen-induced reduction of the cohesive strength of grain boundaries (GBs), while the HELP model is based on the hydrogen-enhanced dislocation mobility. At high tensile triaxialities, the HELP mechanism accelerates the necking failure of microvoids and, at low triaxialities, it induces their shearing coalescence and failure (see e.g., [16,17]). The relevance of HEDE and HELP damage mechanisms should be identified for each particular case of the hydrogen-assisted fracture.

Decohesion processes in polycrystalline metallic materials are mostly restricted to a vicinity of planar defects like grain boundaries and, as a rule, they are affected by a presence of hydrogen and impurity atoms segregating at these defects [18–20]. This was also the case of the H-charged nickel-based superalloy that exhibited quasi-brittle fracture surfaces of a mixed intergranular and transgranular morphology in Ni matrix as reported in the experimental study [1]. Surprisingly, the most frequent crack initiation sites reported by Seita et al. [1] were $\Sigma 3$ coherent twin boundaries, in spite of their lowest energy and hydrogen solubility. Other low- Σ GBs ($\Sigma = 1 - 29$) were less susceptible to crack initiation but less resistant to crack propagation. General GBs ($\Sigma > 29$) exhibited the highest resistance to crack initiation but the lowest resistance to crack propagation. Since the plane of $\Sigma 3$ GB is also the plane of dislocation glide and many of fractured $\Sigma 3$ GBs were inclined by 60° to the tensile axis, the authors assumed that a shear deformation by dislocation glide in the GB plane assisted the crack initiation process, along with dislocations trapped to this plane from other (111) slip planes. Such a damage process resembles the shearing failure induced by the HELP mechanism at low triaxialities [16]. Further crack propagation followed along general grain boundaries due to their highest energy (lowest separation energy and cohesive strength) and the highest hydrogen concentration.

However, such an interpretation of the peculiar fracture behavior is certainly not exhaustive without exploring the effect of hydrogen segregation on the cohesive strength of GBs in H-charged nickel specimens—i.e., without also taking the HEDE mechanism into account. This is the main objective of our ab-initio study. In the first principles calculations, the mechanical properties of GBs are usually characterized by strengthening/embrittling energies [18], cleavage energies (work of separation) [20,21], and/or by the cohesive strength related to uniaxial loading (or deformation). However, GBs in metallic engineering components are rather subjected to an external multiaxial loading/deformation. Moreover, a superposition of local stresses of various kind often leads to a multiaxial stress state, even in the case of uniaxial external loading. Tensile triaxial stresses ahead of crack fronts or tensile/compressive internal stresses induced by thermomechanical and surface treatments can serve as good examples of such local stresses. For the purpose of practical applications of grain boundary engineering, therefore, it is also useful to understand the effect of multiaxial loading on the cohesive strength of GBs. Let us note that cracks not only induce triaxial stress state but also act as stress concentrators that can significantly raise the local stress level.

In this paper, we present values of cohesive strength of clean and hydrogen segregated GBs in fcc nickel. We also studied the aforementioned effect of triaxiality of the stress state on the strength response of GBs in our ab initio predictions. Namely, we studied the $\Sigma 5$, $\Sigma 3$, and $\Sigma 11$ coherent GBs. The $\Sigma 5$ served as an example of GBs with an excess volume (void space) at GBs where impurities tend to segregate. One can therefore expect locally increased hydrogen concentration at the GB affecting its cohesion. The other two considered low-angle GBs have rather negligible excess volume. In such a case, one could expect that these GBs do not affect H distribution in the crystal. However, as was shown in the work of Stefano et al. [7], $\Sigma 3$ GB can serve as a two-dimensional barrier for H migration. Moreover, the GBs included in our study have been studied theoretically and there is enough data for comparison in the literature.

2. Computational Details

The calculations were performed using the program VASP [22] (Vienna ab initio simulation program) developed at the Fakultät für Physik, Universität Wien. In our study, the electron interactions were described by the projector-augmented waves (PAW) potentials [23] supplied with the VASP code, and the exchange correlation energy was evaluated by means of the generalized gradient approximation (GGA) with parametrization of Perdew–Burke–Ernzerhof [24]. The Methfessel–Paxton method of the first order was adopted with a smearing width of 0.1 eV.

Sampling of the Brillouin zone was done using a Monkhorst-Pack [25] scheme with $6 \times 1 \times 10$, $3 \times 1 \times 7$, and $3 \times 1 \times 10$ k -point grids for $\Sigma 3$, $\Sigma 5$, and $\Sigma 11$ GBs, respectively. The solution was

considered self-consistent when the difference between energies of two subsequent steps was below 10^{-7} eV and the plane-wave basis set was expanded with the cutoff energy of 350 eV. Optimization of atomic positions in computational supercells was performed using the internal VASP procedure until all forces between atoms were lower than 10 meV/Å. For the optimization of the cell shape, we employed our own external program that cooperated with VASP via reading its output and writing new input files. This program allowed us to relax the stress tensor components to their targeted values within a tolerance of ± 0.1 GPa. In all presented calculations, ferromagnetic ordering of Ni was included via spin polarization.

Before introducing the studied GBs, let us define two quantities commonly used for their characterization [7,11,26]. The first one is the excess volume v_{exc} , which can be computed as

$$v_{\text{exc}} = \frac{V_{\text{GB}} - N_{\text{GB}}V_{\text{Ni}}}{2A}, \quad (1)$$

where V_{GB} represents the volume, N_{GB} is the number of atoms in a fully optimized supercell containing GB, V_{Ni} is the volume per atom in a perfect bulk crystal of Ni, and A is the GB area. In general, larger values of the excess volume v_{exc} represent more void space at GB. Another important characteristic quantity is the GB energy γ_{GB} determined as

$$\gamma_{\text{GB}} = \frac{E_{\text{GB}} - N_{\text{GB}}E_{\text{Ni}}}{2A}, \quad (2)$$

where the E_{GB} is the total energy of the optimized supercell with GB and E_{Ni} is the total energy per atom of the bulk fcc nickel crystal. Thus, γ_{GB} represents the energy necessary to create such a planar defect of a unit area in a perfect crystal structure. Since all simulation cells contain two identical GBs (as described in the next paragraph), right-hand sides of both equations must be divided by the factor of 2.

In our systematic study, we considered three types of symmetrical GBs in fcc nickel, namely, the $\Sigma 3(111)$ GB, $\Sigma 5(210)$ GB, and the $\Sigma 11(311)$ GB. Corresponding computational supercells that were constructed for the present study are illustrated in Figure 1. These supercells have orthorhombic symmetry and, in order to keep periodic boundary conditions also in the direction perpendicular to the GB plane, they contain two identical GBs. One is located in the center of the supercell and the other one at its edge (displayed as the dashed vertical lines in Figure 1).

All the computational cells were subjected to several types of tensile loading or deformation. Figure 2 illustrates the geometry of our tensile tests. The loading axis is parallel with the x -axis, which was set perpendicular to the GB plane in all our simulations (i.e., $x \parallel [111]$, $x \parallel [210]$, and $x \parallel [311]$ for the $\Sigma 3$, $\Sigma 5$, and $\Sigma 11$ GBs, respectively). Stresses σ_2 and σ_3 are thus the transverse stresses that were controlled by our computational procedure at each strain increment (of 0.01), optimizing both the cell shape and the ionic positions. Since the general loading with $\sigma_2 \neq \sigma_3$ would lead to an enormous number of triaxial stress states (and corresponding values of cohesive strength), we considered these stresses mutually dependent, keeping their ratio $k = \sigma_2/\sigma_3$ constant as discussed hereafter. For $\sigma_2 = \sigma_3 = 0$, the tensile test corresponds to the so-called uniaxial loading. Another special type of loading is the isotropic (or hydrostatic) one with $\sigma_2 = \sigma_1 = \sigma_3$. In this only case, we also controlled the axial stress σ_1 . In all the other cases, we computed σ_1 as a function of the axial strain ϵ_1 . For comparative purposes, we also simulated uniaxial deformation with $\epsilon_2 = \epsilon_3 = 0$ (which implies $\sigma_2 \neq \sigma_3$ due to the crystal anisotropy) and isotropic deformation with $\epsilon_2 = \epsilon_1 = \epsilon_3$. In all applied loading cases, the cohesive strength value was identified with the maximum of σ_1 , hereafter denoted σ_{max} . A brief overview of all loading types is given in Table 1.

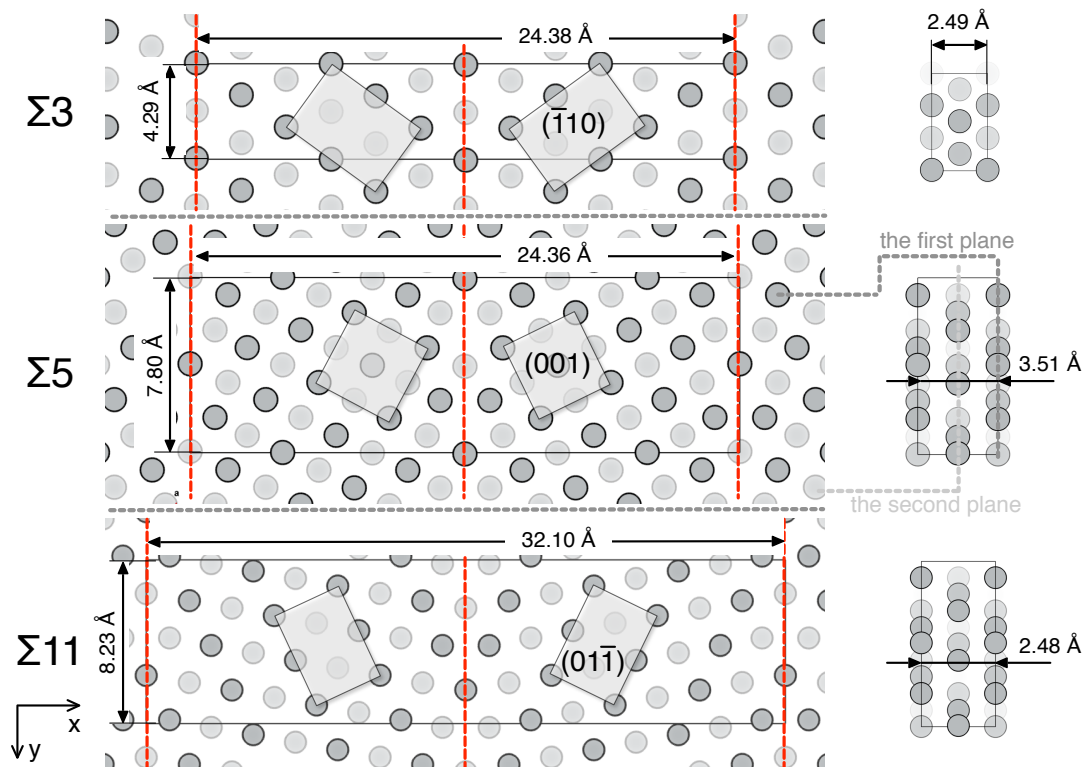


Figure 1. The supercells containing $\Sigma 3(111)$, $\Sigma 5(210)$, and $\Sigma 11(311)$ grain boundaries (GBs) used in the present ab initio calculations. The planes perpendicular to the rotation axis related to GBs are highlighted. Orientation of the supercells were $x \parallel [111]$, $y \parallel [11\bar{2}]$, and $z \parallel [\bar{1}10]$ for the $\Sigma 3$ GB; $x \parallel [210]$, $y \parallel [\bar{1}20]$, and $z \parallel [001]$ for the $\Sigma 5$ GB; and $x \parallel [311]$, $y \parallel [\bar{2}33]$, and $z \parallel [0\bar{1}1]$ for the $\Sigma 11$ GB.

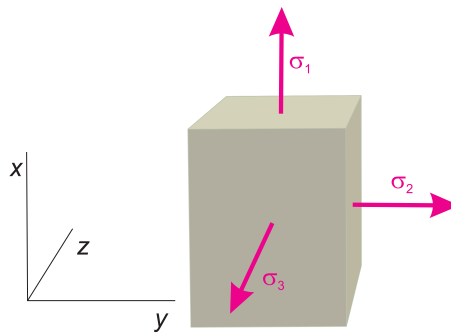


Figure 2. Illustration of the computational supercell under triaxial tensile loading. Stress tensor components are denoted using the Voigt notation.

Table 1. Types of the applied loading.

uniaxial loading	$\sigma_2 = \sigma_3 = 0$
uniaxial deformation	$\epsilon_2 = \epsilon_3 = 0$
triaxial loading	$\sigma_2 = k\sigma_3 \neq 0$
isotropic deformation	$\epsilon_2 = \epsilon_1 = \epsilon_3 \neq 0$
isotropic loading	$\sigma_2 = \sigma_1 = \sigma_3 \neq 0$

3. Results and Discussion

3.1. Structure Parameters of $\Sigma 3$, $\Sigma 5$, and $\Sigma 11$ GBs

3.1.1. Clean Grain Boundaries

All the constructed supercells were fully optimized in order to get their ground-state structures with equilibrium ionic positions and relaxed cell shape and dimensions. The structural parameters received from the optimization process as well as the excess volume v_{exc} and the grain boundary energy γ_{GB} are summarized in Table 2 and compared with available literature data.

Table 2. The excess volume v_{exc} , GB energy γ_{GB} , and the supercell parameters a_0 , b_0 , c_0 of clean $\Sigma 3$, $\Sigma 5$, and $\Sigma 11$ GBs in fcc nickel along with the k -points grid and number N in the simulation cell.

GB		Plane	Rotation Axis	Rotation Angle	v_{exc} (Å)	γ_{GB} (J/m ²)	a_0 (Å)	b_0 (Å)	c_0 (Å)	k-Points Grid	N
$\Sigma 3$	present	{111}	$\langle 110 \rangle$	109.5°	0.02	0.06	24.4	4.29	2.49	1×6×10	24
	Reference [7]				0.05	0.18	24.5	4.32	2.50	1×6×10	24
	Reference [26]				0.01	0.04	-	-	-	1×3×3	-
	Reference [11]				−0.11	0.09	24.3	4.73	4.94	1×4×4	48
$\Sigma 5$	present	{210}	$\langle 001 \rangle$	36.9°	0.26	1.26	24.4	7.81	3.49	1×3×7	60
	Reference [7]				0.38	1.29	16.4	7.93	3.55	2×4×8	40
	Reference [18]				-	1.23	23.6	7.87	3.52	2×6×18	60
	Reference [26]				0.35	1.23	-	-	-	1×3×3	-
	Reference [11]				0.45	1.30	22.9	7.82	6.80	1×3×3	-
$\Sigma 11$	present	{311}	$\langle 100 \rangle$	50.5°	0.08	0.43	32.1	8.23	2.48	1×3×10	60
	Reference [11]				0.06	0.47	21.7	8.22	4.93	1×4×4	80

All the GB parameters agree well with most of the ab initio results formerly published in literature [7,18,26]. Since the $\Sigma 3$ GB is a coherent GB, its volume excess v_{exc} and also the GB energy γ_{GB} are very small (almost zero) and, therefore, these values might be strongly influenced by computational parameters (choice of pseudopotentials, size of computational supercell, etc.) as well as convergence settings during the relaxation process. Note, for example, that v_{exc} computed by Chen et al. [11] is negative but their value of γ_{GB} is in a good agreement with other ab initio results and also with the result $\gamma_{\text{GB}} = 0.05 \text{ J/m}^2$ obtained by Shiga et al. [27] using the embedded atom method (EAM). Values of γ_{GB} computed for the $\Sigma 5$ GB are significantly greater and in a very good mutual agreement. They also reasonably agree with the EAM result [27] of 1.34 eV. The excess volume of the $\Sigma 5$ GB is an order of magnitude greater than that of the $\Sigma 3$. The $\Sigma 11$ GB is also very compact, with very small v_{exc} and relatively low γ_{GB} . Former ab initio [11] as well as EAM calculations [27], giving the γ_{GB} value of 0.40 eV, are in agreement with the present result.

3.1.2. H-Charged Grain Boundaries

The most frequently used strategy to identify the preferred lattice sites for segregation of the hydrogen atoms is usually based on considering several energetically favorable positions (selected with the help of intuition or former experience) at each GB and finding the most favorable one. In the present study, we tested another possible strategy—taking the advantage of the first principles molecular dynamics simulations (FP-MD)—that allowed us to simulate elevated temperatures and to observe a migration of hydrogen atom across the GB. The main advantage of this strategy is the possibility of also finding energetically favorable positions that are not dictated by symmetry and might thus be overlooked in static approaches. Although this approach is more convenient for less-symmetrical GBs than those considered in our study, we decided to test its predictive potential. Moreover, this approach can also indicate positions that can be stabilized by entropy terms at elevated temperatures.

For the present FP-MD simulations, we used a special version of the VASP code compiled for the gamma point only. We enlarged the simulation supercells, repeating those described in Table 2 in the z -direction (in the case of $\Sigma 3$ GB, also in the y -direction) to avoid artificial atomic interactions due to the limited supercell size. Thus, the numbers of Ni atoms in the enlarged supercells were increased to 144, 180, and 180 for $\Sigma 3$, $\Sigma 5$, and $\Sigma 11$ GBs, respectively. To make the simulations feasible, the convergence criterion was reduced to 10^{-5} eV, the cutoff energy was set to 200 eV, and symmetrization of the charge density was switched off. The time step was set to 2 fs. Let us note that lattice parameters of the enlarged supercells were multiplied by the factor of 1.0065 (the atomic positions were set in fractional coordinates), which corresponded to the thermal expansion of a pure nickel from 0 K to 500 K. Then, we introduced a hydrogen atom to the GB and started the FP-MD calculations by a gradual increase in temperature from 0 K to 500 K within the 10,000 time steps, and proceeded with another 10,000 time steps at constant temperature of 500 K.

Hydrogen positions recorded during the constant-temperature range were subjected to a statistical analysis to identify the positions most frequently occupied by the H atom. Results for the $\Sigma 5$ GB (with the highest energy and void space) can be seen from the histogram in Figure 3 displaying the frequency of occurrence of hydrogen atom in positions described by their coordinates (fractional coordinates with respect to the supercell dimensions). The interval on the horizontal axis for a construction of the histogram was set to 1×10^{-3} . The histogram contains only the data for y and z coordinates since the data for the x -coordinate exhibited only one sharp peak at 0.5. To label the preferred segregation sites, we use the same nomenclature (S_x) as Di Stefano et al. [7]. These positions are also marked in Figure 4, displaying the atomic configurations of all GBs. The peaks in Figure 3 reveal the preferred segregation sites labeled S_0 and S_2 .

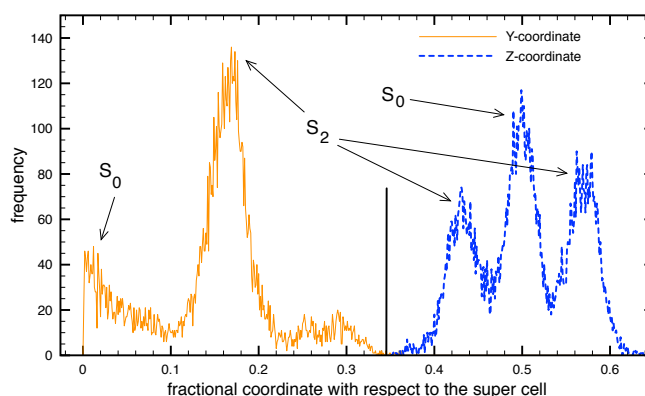


Figure 3. The histogram for the $\Sigma 5$ GB. The solid and dashed lines correspond to frequencies of occurrence of the H atom along the y - and z -coordinates, respectively. The x -coordinate is not shown because there is only one strong peak at 0.5 which corresponds to the GB located in the middle of the supercell. The coordinates are in fractional units of the first principles molecular dynamics simulation (FP-MD) supercell (corresponding to that in Figure 2 repeated three times along z), and the positions S_0 and S_2 are defined in Figure 4.

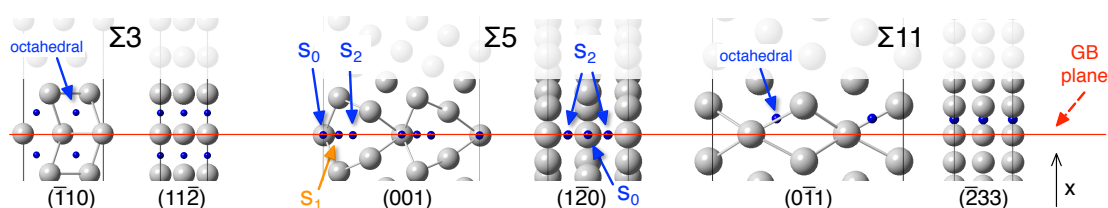


Figure 4. Details of the grain boundary configuration with indicated positions of the preferred segregation sites for hydrogen atoms. S_0 and S_2 are the preferred segregation positions found in the FP-MD simulations, and S_1 is another position considered in Reference [7].

Results for other GBs (though not included in Figure 3) were obtained the same way. Such established hydrogen positions and corresponding segregation energies were compared with those already published by Di Stefano et al. [7]. Since the present nomenclature is consistent, the S_2 positions in both studies are identical. However, instead of the position S_1 reported in [7], we found another position marked S_0 . The segregation energy of -247 meV (-228 meV) obtained for S_0 (S_2) in the present work is close to the value of -230 meV calculated for S_1 in Reference [7]. Alvaro et al. [10] studied preferable hydrogen positions in the $\Sigma 5$ GB and suggested that hydrogen atoms prefer the octahedral-like positions similar to those in the Ni bulk. However, according to our results—as well as the work of Di Stefano et al. [7] (where these positions were marked as S_6 and S_7)—their segregation energies are higher than the energies of S_1 and S_2 .

The hydrogen segregation for the remaining GBs of a smaller energy and void space is significantly reduced when compared to $\Sigma 5$. According to the FP-MD results obtained for $\Sigma 3$ and $\Sigma 11$ GBs, the hydrogen atoms tend to segregate only at octahedral sites near the GB planes. These positions are depicted in Figure 4 and marked by small (blue) spheres representing the segregated hydrogen atoms. This figure shows the hydrogen occupation sites for all three studied GB supercells that were used for the determination of cohesive strengths.

3.2. Cohesive Strength of Hydrogen-Free GBs

The computational tensile tests were first performed for a perfect crystal of Ni loaded in crystallographic directions corresponding to the orientations of the loading axes in GB models (perpendicular to the GB planes), i.e., $\langle 111 \rangle$, $\langle 210 \rangle$, and $\langle 311 \rangle$ for $\Sigma 3$, $\Sigma 5$, and $\Sigma 11$, respectively. We started with the uniaxial deformation keeping the transverse lattice parameters constant (see Table 1) and computed all the normal stresses as functions of the axial strain ϵ_1 . The results are displayed in Figure 5, where the transverse stresses σ_2 , σ_3 are plotted as functions of the axial stress σ_1 up to σ_{\max} .

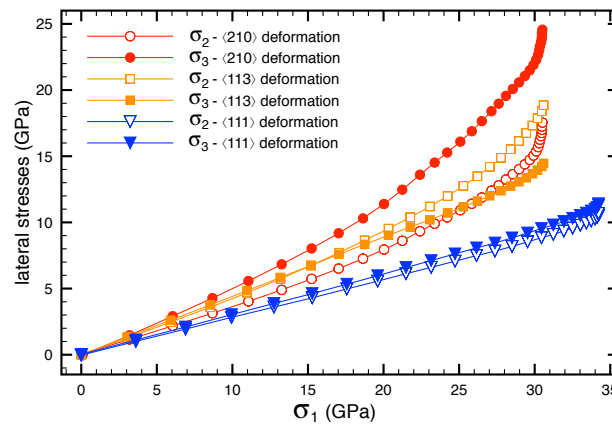


Figure 5. The relationship between the transverse stresses σ_2 , σ_3 and the axial stress σ_1 computed for the uniaxial deformation of bulk fcc Ni in the $\langle 111 \rangle$, $\langle 210 \rangle$, and $\langle 311 \rangle$ crystallographic directions.

One can note that omitting the Poisson contraction during the uniaxial deformation induces tensile transverse stresses that are superimposed to σ_1 , thus making the stress state triaxial. Values of σ_2 and σ_3 generally differ. They depend not only on the particular orientation of the x -axis but also on anisotropy of the perpendicular ($\{111\}$, $\{210\}$, and $\{311\}$) atomic planes. Therefore, we respected this anisotropy by keeping the same ratios σ_3/σ_2 also in the cases of triaxial loading (see Table 1) applied to supercells simulating perfect crystals as well as the crystals with GBs. The greatest ratio $\sigma_3/\sigma_2 = 1.4$ was obtained for the $[210]$ direction, i.e., the same ratio was used in the triaxial tensile tests of supercells with the $\Sigma 5$ GB. The ratio obtained for the $[111]$ deformation is approximately equal to 1, thus, this ratio was also used for the triaxial tensile tests of $\Sigma 3$ GB. The response of Ni crystal elongated in the $\{311\}$ direction is somewhat complicated. For smaller strains (and the σ_1 values slightly above 15 GPa),

the ratio is close to 1.0, but for greater strains (and the stresses close to the σ_{\max} value) it decreases to $\sigma_3/\sigma_2 = 0.8$. The latter value was selected for the triaxial loading of $\Sigma 11$ GB since the ratio close to the σ_{\max} value is of a higher relevance.

The tensile tests for all the loading conditions listed in Table 1 were then applied to the optimized GBs and the computed data are summarized in Figure 6. The left panel displays results of the triaxial loading in terms of the cohesive strength value σ_{\max} as a function of the applied transverse stress σ_2 for each GB model and the crystallographic direction. The right panel of Figure 6 shows the results received for special loading cases: uniaxial deformation, isotropic loading, and isotropic deformation.

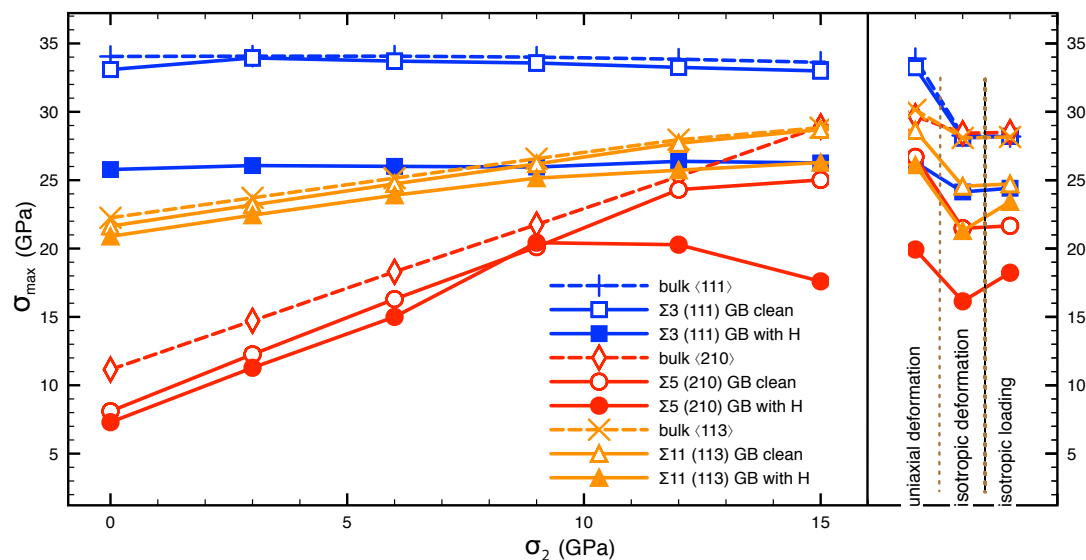


Figure 6. Computed values of the cohesive strength σ_{\max} for the bulk crystal (symbols connected by dashed lines), clean GB (open symbols, solid lines), and H-charged GB (solid symbols, solid lines). The left panel shows σ_{\max} as a function of one of the transverse stresses (σ_2) during triaxial loading. The right panel displays the σ_{\max} values computed for other specific loading types. Note that the data for $\sigma_2 = 0$ correspond to results of uniaxial loading.

The results shown in the left panel of Figure 6 reveal that σ_{\max} for $\Sigma 5$ and $\Sigma 11$ GBs linearly increases with increasing transverse stresses (as already reported for a majority of perfect cubic crystals and loading directions [28]), while it remains constant for the $\Sigma 3$ GB and the bulk Ni crystal loaded in the [111] direction. Such an insensitivity to the superimposed transverse stresses is also indicated by the value of σ_{\max} achieved via uniaxial deformation that is practically equal to σ_{\max} from uniaxial loading (i.e., the value in the left panel of Figure 6 for $\sigma_2 = 0$).

One can also see that σ_{\max} values of the bulk crystal loaded in the crystallographic directions corresponding to orientations of grains in individual GBs (plotted in Figure 6 by symbols connected by dashed lines) mostly follow the values computed for the related GBs. In the cases of $\Sigma 3$ (111) and $\Sigma 11$ (311) GBs, values for the bulk and clean GB are almost equal (naturally, with slightly higher σ_{\max} values for the bulk crystal). This means that the presence of $\Sigma 3$ and $\Sigma 11$ GBs practically does not reduce the crystal strength. More remarkable reduction of σ_{\max} is caused by the presence of $\Sigma 5$ (210) GB.

The right panel in Figure 6 shows that the isotropic (hydrostatic) loading as well as the isotropic deformation yield lower σ_{\max} values than the uniaxial deformation. Let us note that, in the case of bulk crystals, both the isotropic loading and the isotropic deformation must lead to the same σ_{\max} value, regardless of the orientation of the loading axis. The corresponding data points (each obtained using a differently oriented supercell or deformation model) displayed in Figure 6 confirm reliability of our computational procedures by their negligible differences. Interestingly, almost the same values were also obtained for the supercell with the clean $\Sigma 3$ GB, thus indicating that its effect on crystal strength can be considered negligible. On the other hand, presence of the other two GBs (with higher

energy γ_{GB}) significantly reduce σ_{max} under isotropic tensile loading. Therefore, one can presume that the cohesive strength of general GBs exhibiting greater GB energy will be even more reduced, particularly for highly triaxial stress states.

3.3. Cohesive Strength of Hydrogen-Charged GBs

The influence of hydrogen segregation on the cohesive strength was then studied using supercells charged with the hydrogen. Its amount introduced to the supercell was 4, 6, and 2 atoms for $\Sigma 3$, $\Sigma 5$, and $\Sigma 11$ GBs, respectively. These numbers correspond to an optimum coverage (all available interstitial positions are filled with hydrogen) but also to a locally-enhanced hydrogen concentration (much greater than can be expected for the rest of the crystal).

The supercells were subjected to tensile tests with all the considered loading conditions and the results were added to Figure 6. The H-charged $\Sigma 3$ GB again exhibits a quite different strength response than the other two GB types. Similarly to the results for hydrogen-free GBs, the cohesive strengths of $\Sigma 5$ and $\Sigma 11$ GBs increased with increasing transverse stresses while the value of the cohesive strength of $\Sigma 3$ GB remained constant in the whole range of the transverse stresses. More interestingly however, the cohesive strength of $\Sigma 3$ was distinctly reduced for all levels of the superimposed transverse stresses. The strength reduction for $\Sigma 5$ and $\Sigma 11$ GBs was significant only in the case of high biaxial stresses, i.e., for nearly isotropic (hydrostatic) loading cases.

To understand the effect of the compact $\Sigma 3$ GB (with a negligible excess volume) in the H-charged crystal, we also computed the tensile strength of H-charged bulk Ni (perfect crystal) subjected to uniaxial deformation along the $[111]$ direction. As can be seen from Figure 6, the strength values for the clean bulk and the $\Sigma 3$ GB are very similar (33.9 GPa and 33.2 GPa, respectively). After introducing H to the $\Sigma 3$ GB, the strength decreased to 26.3 GPa, but the same amount of H introduced to the perfect lattice (using comparable supercell) reduced the strength only to 28.6 GPa. This suggests that the higher strength reduction of $\Sigma 3$ GB than that of the perfect lattice is caused by an interaction of H atoms that get closer to each other in the $\Sigma 3$ GB than in the perfect lattice. The values of cohesive strength are seemingly too high in comparison with typical levels of stress applied to the specimen in the instant of first occurrence of cracks. However, one must bear in mind that, due to the presence of stress concentrators, local stress levels are much higher and can reach the computed strength values.

Thus, our study reveals strong additional HEDE-based reasons for the highest susceptibility of special $\Sigma 3$ GBs to crack initiation, as well as for the lowest resistance of general GBs to crack propagation during uniaxial loading. Indeed, the presence of hydrogen reduces the cohesive strength of $\Sigma 3$ GBs to become closer to strength levels of special GBs which remain hydrogen-unaaffected. Therefore, along with the movement and interaction of dislocations in the $\Sigma 3$ GB plane, such a decrease in the cohesive strength makes the $\Sigma 3$ GB plane a comprehensible preferential site for nucleation of microcracks. Once these cracks appear in the $\Sigma 3$ GB planes, the cohesive strength of other types of GBs adjacent to $\Sigma 3$ GBs also becomes reduced due to a highly triaxial tensile loading induced in the vicinity of the microcrack networks. Naturally, a further crack propagation preferentially occurs along general grain boundaries which exhibit the lowest cohesive strength and the highest hydrogen concentrations. The most probable fracture scenario of nickel polycrystal in the hydrogen environment is, therefore, a result of both HELP and HEDE damage mechanisms.

3.4. Work of Separation

Work of separation W_{oS} (also called cleavage energy or cohesive energy) is another quantity which can be (and often is) used to characterize the GB cohesion. It is calculated as an energy necessary to break the crystal along a specified cleavage plane, as expressed by the following formula

$$W_{oS} = \frac{E_{FS(+H)} - E_{GB(+H)}}{A}, \quad (3)$$

where $E_{\text{GB}(+\text{H})}$ is the total energy of the fully optimized supercell containing the GB (with or without hydrogen atoms), E_{FS} is the total energy of a supercell with two free surfaces (i.e., the fractured supercell), and A is the GB cross-section area. As has been formerly discussed [19,29], selection of the weakest cleavage (or fracture) plane is of key importance. There is no doubt about its position in the case of a clean GB but, in the case of H-decorated GB, one must consider possible redistribution of hydrogen on the created surfaces since it affects the $E_{\text{FS}(+\text{H})}$ value. Our choice was based on the result of the tensile tests, namely, the uniaxial deformation which keeps the transverse dimensions constant and, therefore, is consistent with typical W_{OS} calculations. Values computed for GB configurations in Figure 4 are listed in Table 3. To illustrate the effect of surface relaxation, we list the values for both the unrelaxed (as created) and the relaxed surfaces (relaxation reduces the value of $E_{\text{FS}(+\text{H})}$ in Equation (3)).

Table 3. Work of separation (in J/m²) calculated for $\Sigma 3$, $\Sigma 5$, and $\Sigma 11$ GBs with and without hydrogen.

GB	Unrelaxed		Relaxed	
	Clean	With H	Clean	With H
$\Sigma 3(111)$	3.78	2.77	3.76	2.34
$\Sigma 5(210)$	4.00	3.41	3.59	1.82
$\Sigma 11(311)$	4.35	3.76	4.15	3.37

Despite the fact that the $\Sigma 3$ GB exhibits the greatest strength values (see Figure 6), its W_{OS} values for unrelaxed surfaces are lower than values computed for the other GBs. The greatest W_{OS} values were obtained for the $\Sigma 11$ GB. These values fall within the range of results of fracture energies computed by Tehranchi and Curtin [12] for seven other GBs.

Let us note that values of the work of separation for bulk differ from the W_{OS} values in Table 3 only by the GB energy (γ_{GB} in Table 2), and one can therefore easily calculate the surface energy $\gamma_{\text{FS}} = (W_{\text{OS}} + \gamma_{\text{GB}})/2$. Values of 2.43 J/m² for (210) and 1.91 J/m² for (111) surfaces obtained this way (using the relaxed W_{OS} values) agree well with the values of 2.40 J/m² and 1.92 J/m² reported by Tran et al. [30].

Alvaro et al. [10] and Chen et al. [11] calculated the work of separation for clean and H-charged GBs in Ni using a relationship differing from Equation (3) by a factor of 2 (the definition corresponded rather to the surface energy), therefore their values correspond to one half of our W_{OS} in Table 3. Values of 1.88 J/m² [10] and 1.86 J/m² [11] determined for the clean $\Sigma 3$ GB therefore agree very well with our results of relaxed calculations. In addition, the values of 1.75 J/m² [11] and 1.8 J/m² [10] for the clean $\Sigma 5$ GB and 2.04 J/m² [11] for the clean $\Sigma 11$ GB are in agreement with data in Table 3.

For H-charged GBs in fcc Ni, Chen et al. [11] predicted a complete decohesion of the $\Sigma 3$ GB fully covered with hydrogen atoms (forming a monolayer), since their relevant W_{OS} value was almost zero. However, our tensile tests predict only a reduction of the tensile strength (for loading of any kind). Our W_{OS} values in Table 3 also show that the presence of one hydrogen monolayer at the $\Sigma 3$ GB reduces its W_{OS} by one third. Although such a relative reduction of W_{OS} is greater than that of σ_{max} , it does not predict the catastrophic crystal decohesion reported in Reference [11]. Instead, it agrees much better with the value of 1.1 J/m² published by Alvaro et al. [10].

4. Conclusions

This article presents an ab initio study of the cohesive strength of selected types of special grain boundaries in hydrogen-free and hydrogen-charged nickel crystals under uniaxial and triaxial loading. The main motivation was to find out if not only the dislocation HELP mechanism, but also the HEDE might have been responsible for experimentally observed high susceptibility of $\Sigma 3$ coherent twin boundaries to crack initiation. The results indeed revealed that the presence of hydrogen reduces the cohesive strength of $\Sigma 3$ boundaries to become closer to strength levels of higher-energy GBs which, in contrary, remain hydrogen-unaffected. Thus, this HEDE (decohesion) mechanism makes, along with

the previously reported dislocation (HELP) mechanism, the $\Sigma 3$ GB plane a comprehensible preferential site for nucleation of microcracks. The results of this study also brought an additional HEDE-based explanation of a small resistance of higher-energy GBs to crack propagation. The highly-triaxial stress state at the tips of microcracks (initiated at $\Sigma 3$ boundaries) caused an extreme reduction of cohesive strength of adjacent high-energy grain boundaries, especially those of a general kind.

Author Contributions: Conceptualization, J.P. and Z.Z.; methodology, P.Š. and M.Č.; ab initio calculations, P.Š.; formal analysis, M.Č. and J.P.; writing—original draft preparation, P.Š.; writing—review and editing, J.P., M.Č., and Z.Z.; visualization, P.Š. and M.Č.; supervision, J.P.; funding acquisition, J.P. and M.Č. All authors have read and agreed to the published version of the manuscript.

Funding: This research was supported by the Czech Science Foundation (projects No. 17-18566S and No. 20-08130S) and by the Ministry of Education, Youths and Sports of the Czech Republic within special support paid from the National Programme for Sustainability II funds within CEITEC 2020 (project No. LQ1601). Z.Z. would like to thank the Research Council of Norway for the support via the M-HEAT (294689) and HyLine project. Computational resources were provided by the Ministry of Education, Youths and Sports of the Czech Republic under the Project IT4Innovations National Supercomputer Center (Project No. LM2015070) within the program Projects of Large Research, Development and Innovations Infrastructures.

Conflicts of Interest: The authors declare no conflict of interest.

References

- Seita, M.; Hanson, J.P.; Gradečák, S.; Demkowicz, M.J. The dual role of coherent twin boundaries in hydrogen embrittlement. *Nat. Commun.* **2015**, *6*, 6164. [[CrossRef](#)] [[PubMed](#)]
- Koyama, M.; Tasan, C.C.; Akiyama, E.; Tsuzaki, K.; Raabe, D. Hydrogen-assisted decohesion and localized plasticity in dual-phase steel. *Acta Mater.* **2014**, *70*, 174–187. [[CrossRef](#)]
- Geng, W.T.; Freeman, A.J.; Wu, R.; Geller, C.B.; Raynolds, J.E. Embrittling and strengthening effects of hydrogen, boron, and phosphorus on a $\Sigma 5$ nickel grain boundary. *Phys. Rev. B* **1999**, *60*, 7149–7155. [[CrossRef](#)]
- Xu, X.; Wen, M.; Hu, Z.; Fukuyama, S.; Yokogawa, K. Atomistic process on hydrogen embrittlement of a single crystal of nickel by the embedded atom method. *Comput. Mater. Sci.* **2002**, *23*, 131–138. [[CrossRef](#)]
- Wen, M.; Xu, X.J.; Omura, Y.; Fukuyama, S.; Yokogawa, K. Modeling of hydrogen embrittlement in single crystal Ni. *Comput. Mater. Sci.* **2004**, *30*, 202–211. [[CrossRef](#)]
- Tahir, A.; Janisch, R.; Hartmaier, A. Hydrogen embrittlement of a carbon segregated symmetrical tilt grain boundary in α -Fe. *Mater. Sci. Eng. A* **2014**, *612*, 462–467. [[CrossRef](#)]
- Di Stefano, D.; Mrovec, M.; Elsässer, C. First-principles investigation of hydrogen trapping and diffusion at grain boundaries in nickel. *Acta Mater.* **2015**, *98*, 306–312. [[CrossRef](#)]
- Yamaguchi, M.; Shiga, M.; Kaburaki, H. First-Principles Study on Segregation Energy and Embrittling Potency of Hydrogen in $\text{Ni}\Sigma 5(012)$ Tilt Grain Boundary. *J. Phys. Soc. Jpn.* **2004**, *73*, 441–449. [[CrossRef](#)]
- Yu, H.; Olsen, J.S.; Alvaro, A.; Olden, V.; He, J.; Zhang, Z. A uniform hydrogen degradation law for high strength steels. *Eng. Fract. Mech.* **2016**, *157*, 56–71. [[CrossRef](#)]
- Alvaro, A.; Jensen, I.T.; Kheradmand, N.; Løvvik, O.; Olden, V. Hydrogen embrittlement in nickel, visited by first principles modeling, cohesive zone simulation and nanomechanical testing. *Int. J. Hydrog. Energy* **2015**, *40*, 16892–16900. [[CrossRef](#)]
- Chen, J.; Dongare, A.M. Role of grain boundary character on oxygen and hydrogen segregation-induced embrittlement in polycrystalline Ni. *J. Mater. Sci.* **2017**, *52*, 30–45. [[CrossRef](#)]
- Tehranchi, A.; Curtin, W.A. Atomistic study of hydrogen embrittlement of grain boundaries in nickel: II. Decohesion. *Modell. Simul. Mater. Sci. Eng.* **2017**, *25*, 075013. [[CrossRef](#)]
- He, S.; Ecker, W.; Pippan, R.; Razumovskiy, V.I. Hydrogen-enhanced decohesion mechanism of the special $\Sigma 5(012)[100]$ grain boundary in Ni with Mo and C solutes. *Comput. Mater. Sci.* **2019**, *167*, 100–110. [[CrossRef](#)]
- Oriani, R.A. A mechanistic theory of hydrogen embrittlement of steels. *Berichte Bunsenges. Phys. Chem.* **1972**, *76*, 848–857. [[CrossRef](#)]
- Birnbaum, H.; Sofronis, P. Hydrogen-enhanced localized plasticity—A mechanism for hydrogen-related fracture. *Mater. Sci. Eng. A* **1994**, *176*, 191–202. [[CrossRef](#)]

16. Yu, H.; Olsen, J.S.; He, J.; Zhang, Z. Hydrogen-microvoid interactions at continuum scale. *Int. J. Hydrog. Energy* **2018**, *43*, 10104–10128. [[CrossRef](#)]
17. Zhao, K.; He, J.; Mayer, A.; Zhang, Z. Effect of hydrogen on the collective behavior of dislocations in the case of nanoindentation. *Acta Mater.* **2018**, *148*, 18–27. [[CrossRef](#)]
18. Všianská, M.; Šob, M. The effect of segregated *sp*-impurities on grain-boundary and surface structure, magnetism and embrittlement in nickel. *Prog. Mater. Sci.* **2011**, *56*, 817–840. [[CrossRef](#)]
19. Černý, M.; Šesták, P.; Řehák, P.; Všianská, M.; Šob, M. Ab initio tensile tests of grain boundaries in the fcc crystals of Ni and Co with segregated *sp*-impurities. *Mater. Sci. Eng. A* **2016**, *669*, 218–225. [[CrossRef](#)]
20. Tahir, A.M.; Janisch, R.; Hartmaier, A. Ab initio calculation of traction separation laws for a grain boundary in molybdenum with segregated C impurities. *Modell. Simul. Mater. Sci. Eng.* **2013**, *21*, 075005. [[CrossRef](#)]
21. Janisch, R.; Ahmed, N.; Hartmaier, A. Ab initio tensile tests of Al bulk crystals and grain boundaries: Universality of mechanical behavior. *Phys. Rev. B* **2010**, *81*, 184108. [[CrossRef](#)]
22. Kresse, G.; Furthmüller, J. Efficient iterative schemes for ab initio total-energy calculations using a plane-wave basis set. *Phys. Rev. B* **1996**, *54*, 11169–11186. [[CrossRef](#)]
23. Kresse, G.; Joubert, D. From ultrasoft pseudopotentials to the projector augmented-wave method. *Phys. Rev. B* **1999**, *59*, 1758–1775. [[CrossRef](#)]
24. Perdew, J.P.; Burke, K.; Ernzerhof, M. Generalized Gradient Approximation Made Simple. *Phys. Rev. Lett.* **1996**, *77*, 3865–3868. [[CrossRef](#)]
25. Monkhorst, H.J.; Pack, J.D. Special points for Brillouin-zone integrations. *Phys. Rev. B* **1976**, *13*, 5188–5192. [[CrossRef](#)]
26. Bean, J.J.; McKenna, K.P. Origin of differences in the excess volume of copper and nickel grain boundaries. *Acta Mater.* **2016**, *110*, 246–257. [[CrossRef](#)]
27. Shiga, M.; Yamaguchi, M.; Kaburaki, H. Structure and energetics of clean and hydrogenated Ni surfaces and symmetrical tilt grain boundaries using the embedded-atom method. *Phys. Rev. B* **2003**, *68*, 245402. [[CrossRef](#)]
28. Černý, M.; Pokluda, J. Ideal tensile strength of cubic crystals under superimposed transverse biaxial stresses from first principles. *Phys. Rev. B* **2010**, *82*, 174106. [[CrossRef](#)]
29. Černý, M.; Šesták, P.; Řehák, P.; Všianská, M.; Šob, M. Atomistic approaches to cleavage of interfaces. *Modell. Simul. Mater. Sci. Eng.* **2019**, *27*, 035007. [[CrossRef](#)]
30. Tran, R.; Xu, Z.; Radhakrishnan, B.; Winston, D.; Sun, W.; Persson, K.A.; Ong, S.P. Surface energies of elemental crystals. *Sci. Data* **2016**, *3*, 160080. [[CrossRef](#)]



© 2020 by the authors. Licensee MDPI, Basel, Switzerland. This article is an open access article distributed under the terms and conditions of the Creative Commons Attribution (CC BY) license (<http://creativecommons.org/licenses/by/4.0/>).